



Constructing “Li-rich Ni-rich” oxide cathodes for high-energy-density Li-ion batteries

Biao Li, Gwenaëlle Rousse, Leiting Zhang, Maxim Avdeev, Michaël Deschamps, Artem Abakumov, Jean-Marie Tarascon

► To cite this version:

Biao Li, Gwenaëlle Rousse, Leiting Zhang, Maxim Avdeev, Michaël Deschamps, et al.. Constructing “Li-rich Ni-rich” oxide cathodes for high-energy-density Li-ion batteries. *Energy & Environmental Science*, 2023, 16 (3), pp.1210-1222. 10.1039/D2EE03969A . hal-04047592v1

HAL Id: hal-04047592

<https://hal.science/hal-04047592v1>

Submitted on 27 Mar 2023 (v1), last revised 7 Apr 2023 (v2)

HAL is a multi-disciplinary open access archive for the deposit and dissemination of scientific research documents, whether they are published or not. The documents may come from teaching and research institutions in France or abroad, or from public or private research centers.

L'archive ouverte pluridisciplinaire **HAL**, est destinée au dépôt et à la diffusion de documents scientifiques de niveau recherche, publiés ou non, émanant des établissements d'enseignement et de recherche français ou étrangers, des laboratoires publics ou privés.

Constructing “Li-rich Ni-rich” oxide cathodes for high-energy-density Li-ion batteries

Biao Li^{1,2}, Gwenaëlle Rousse^{1,2,3}, Leiting Zhang⁴, Maxim Avdeev^{5,6}, Michaël Deschamps^{2,7}, Artem M. Abakumov⁸, Jean-Marie Tarascon^{1,2,3*}

¹Chimie du Solide-Energie, UMR 8260, Collège de France, 75231 Paris Cedex 05, France.

²Réseau sur le Stockage Electrochimique de l’Energie (RS2E), FR CNRS 3459, France.

³Sorbonne Université, 4 Place Jussieu, 75005, Paris, France.

⁴Battery Electrodes and Cells, Electrochemistry Laboratory, Paul Scherrer Institute, Forschungsstrasse 111, 5232 Villigen-PSI, Switzerland. (*Present address: Department of Chemistry – Ångström Laboratory, Uppsala University, Box 538, SE-751 21 Uppsala, Sweden.*)

⁵School of Chemistry, The University of Sydney, Sydney, New South Wales, Australia.

⁶Australian Centre for Neutron Scattering, Australian Nuclear Science and Technology Organisation, Kirrawee DC, New South Wales, Australia.

⁷CNRS, CEMHTI UPR3079, Université d’Orléans, Orléans, France

⁸Center for Energy Science and Technology, Skolkovo Institute of Science and Technology, Nobel str. 3, 121205 Moscow, Russia.

* Corresponding author: jean-marie.tarascon@college-de-france.fr

Key words: Li-ion batteries, Li-rich, Ni-rich, layered, disordered

Abstract

The current exploration of high-energy-density cathode materials for Li-ion batteries is mainly concentrated on either so-called “Li-rich” or “Ni-rich” oxides. However, both are suffering from formidable practical challenges. Here, we combine these two concepts to obtain “Li-rich Ni-rich” oxides in pursuit of more practical high-energy-density cathodes. As a proof of concept, we synthesized an array of $\text{Li}_{1+y}\text{Ni}_{(3-5y)/3}\text{Mo}_{2y/3}\text{O}_2$ oxides, whose structures were identified to be the coexistence of LiNiO_2 -rich and Li_4MoO_5 -rich domains with the aid of XRD, TEM, and NMR techniques. Such intergrowth structure with 5-20 nm in size enables excellent mechanical and structural reversibility for the layered rock-salt LiNiO_2 -rich domain upon cycling thanks to the robust cubic rock-salt Li_4MoO_5 -rich domain enabling an “epitaxial stabilization” effect. As a result, we achieved high capacities ($>220 \text{ mA h g}^{-1}$) with Ni contents as low as 80%; the $\text{Li}_{1.09}\text{Ni}_{0.85}\text{Mo}_{0.06}\text{O}_2$ member ($y = 0.09$) shows much improved cycling performances (91% capacity retention for 100 cycles at C/10) compared with pure LiNiO_2 . This work validates the feasibility of constructing Li-rich Ni-rich compounds in a form of intergrowing domains and hence unlocks vast possibilities for future cathode design.

Introduction

The electric vehicles (EVs) market is under rapid growth, as witnessed by the number of EVs on the roads that has set a new record (>10 millions) at the end of 2020¹. The prosperity of the EV market is driving the demand for high-energy-density Li-ion batteries acting as power sources. Throughout the past decades, enormous efforts have been devoted to exploring potential candidates for both cathodes and anodes in pursuit of higher energy densities. Among them, classical cathode candidates, such as LiCoO_2 , LiFePO_4 , and $\text{LiNi}_{1/3}\text{Co}_{1/3}\text{Mn}_{1/3}\text{O}_2$, primarily suffer from low capacities, typically below 200 mA h g^{-1} and, therefore, low energy densities.² Hence, practical high-energy-density electrodes are pressingly demanded.

The current exploration of high-energy-density cathode materials is ongoing along two routes. The first concerns the so-called Li-rich materials, $\text{Li}_{1+x}\text{M}_{1-x}\text{O}_2$ (M denotes transition metal hereafter), with additional Li ions partially replacing M ions at the transition metal layer.³ They can provide exceptionally high capacities ($>250 \text{ mA h g}^{-1}$) stemming from anionic redox phenomenon, a paradigm-shift concept that is receiving worldwide attentions⁴⁻⁷. However, this class of materials are plagued by their common shortcomings such as voltage hysteresis and voltage fade brought forward by the aforementioned anionic redox, and their prospect of practical use remains unclear unless these bottlenecks are overcome^{4,8}.

In parallel, the community is also striving on another strategy — the so-called Ni-rich (or high-Ni) oxides with either the $\text{LiNi}_x\text{Co}_y\text{Mn}_{1-x-y}\text{O}_2$ (NMC) or $\text{LiNi}_x\text{Co}_y\text{Al}_{1-x-y}\text{O}_2$ (NCA) compositions with x typically equal or larger than 0.8.^{9,10} They are derived from LiNiO_2 and are generating great interest owing to their high capacities ($> 200 \text{ mA h g}^{-1}$) and high working potentials ($\sim 3.8 \text{ V}$). However, these Ni-rich electrodes are suffering from mechanical, electrochemical and thermal stability issues that, in some extent, limit their commercial use.¹¹ Therefore, our society is in dire need of new strategies for circumventing such weaknesses while keeping or even increasing the cathode capacity.

In this work, we aim to explore the feasibility of merging the Li-rich concept into the Ni-rich oxide materials as a potential solution of the dilemma mentioned above. This idea was initiated by the fact that placing additional Li ions in Ni layer should create O 2p non-bonding states that can serve as an additional redox reservoir, which can buffer the electron depletion from σ -type $\text{Ni}(3d)\text{-O}(2p)$ hybridized states that was supposed to cause the devastation of oxygen framework.¹²⁻¹⁴ Besides, the replacement of Ni by Li will also increase the theoretical

capacity and reduce the Ni content in order to get rid of the stability issues. As Li^+ is less positively charged than Ni^{3+} , such design strategy implies the need to introduce another high-valence metal ion, such as Mo^{6+} , W^{6+} , Nb^{5+} , and Mn^{4+} , to balance the charge. The introduction of these redox inactive metal ions can also benefit the stabilization of the structure, as frequently suggested by previous works¹⁵⁻¹⁷.

We herein implement this strategy by placing additional Li^+ and Mo^{6+} ions, as a proof of concept, into LiNiO_2 , to generate an array of Li-rich Ni-rich materials that can be nominally formulated as $\text{Li}_{1+y}\text{Ni}_{(3-5y)/3}\text{Mo}_{2y/3}\text{O}_2$ ($y=0.03, 0.06, 0.09$, and 0.12). We found that these materials, instead of forming solid solutions, are composed of layered LiNiO_2 -based domains and Li_4MoO_5 -based disordered rock-salt domains intergrown together, as evidenced by synchrotron X-ray powder diffraction (SXRD), neutron powder diffraction (NPD), transmission electron microscopy (TEM) and nuclear magnetic resonance (NMR) studies. As a result, these Li-rich Ni-rich composites show comparable and even higher capacities ($210\sim 230\text{ mA h g}^{-1}$), even with Ni contents as low as 80%, compared with that of pure LiNiO_2 (220 mA h g^{-1}), with some of them showing excellent cycling stabilities as well.

Results and discussions

General structural characterizations. $\text{Li}_{1+y}\text{Ni}_{(3-5y)/3}\text{Mo}_{2y/3}\text{O}_2$ ($y=0.03, 0.06, 0.09$, and 0.12) were synthesized via a solution-preceded solid-state process (the details can be found in the experimental section). The elemental compositions were checked by inductively coupled plasma atomic emission spectroscopy (ICP-AES), showing Li/Ni ratios consistent with the nominal ones (Table S1). However, Mo contents were found to be far below the theoretical values, which is due to the Mo oxides (e.g. MoO_3) have limited solubility in acidic media especially when aqua regia was used for ICP-AES measurements¹⁸. Scanning electron microscopy (SEM) coupled with energy dispersive X-ray analysis (EDX) was further employed to validate the Ni/Mo ratios, as tabulated in Table S2, showing good consistency with the nominal values.

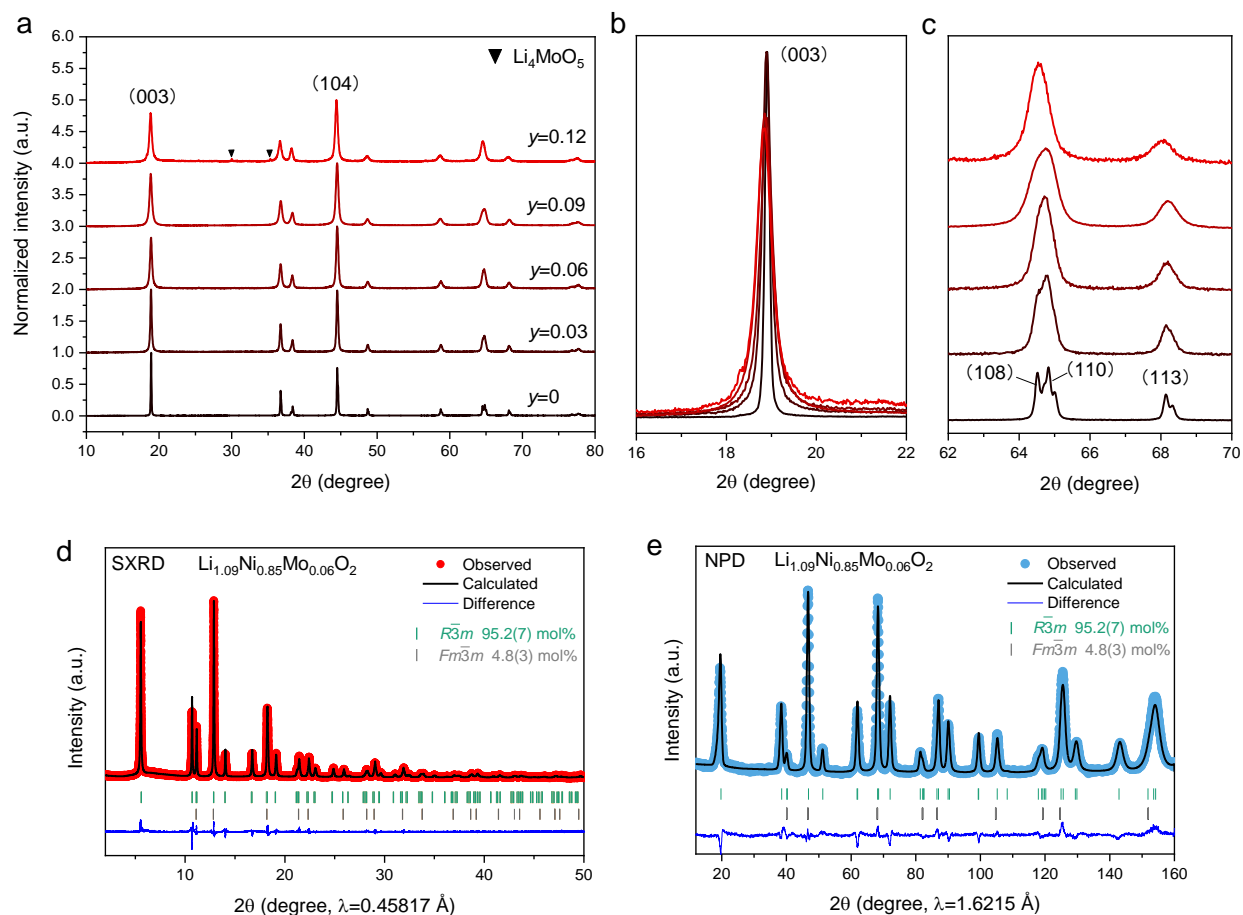


Figure 1. Structural characterizations of $\text{Li}_{1+y}\text{Ni}_{(3-5y)/3}\text{Mo}_{2y/3}\text{O}_2$ ($y=0, 0.03, 0.06, 0.09, 0.12$). (a) XRD patterns. (b)(c) Enlarged parts of XRD patterns. (d)(e) Combined Rietveld refinement results of SXRD and NPD for the $y=0.09$ member ($\text{Li}_{1.09}\text{Ni}_{0.85}\text{Mo}_{0.06}\text{O}_2$). The refinement was done with a two-phase model with $\text{Li}_{1.04}\text{Ni}_{0.93}\text{Mo}_{0.03}\text{O}_2$ ($R\bar{3}m$) and Li_4MoO_5 ($Fm\bar{3}m$) whose molar percentage was indicated. The color-coded vertical bars are the Bragg positions of each phase.

X-ray powder diffraction (XRD) was further employed to investigate the structures of the as-synthesized $\text{Li}_{1+y}\text{Ni}_{(3-5y)/3}\text{Mo}_{2y/3}\text{O}_2$ samples. As shown in Fig. 1a, LiNiO_2 is well crystallized in a typical layered structure with $R\bar{3}m$ symmetry in line with what has been reported previously¹⁹. Upon the addition of Li and Mo, the diffraction peaks are getting broader as observed from the evolution of (003) peak (Fig. 1b) and (108), (110) peaks (Fig. 1c). This indicates a decrease of the crystallite sizes, as identified by the SEM images (Fig. S1), with probably also an increasing degree of the micro-strain. Besides, the lattice parameter a and c , obtained via Rietveld refinement, generally increase as a function of Li content (Fig. S2). Such lattice expansion suggests the successful incorporation into the LiNiO_2 lattice of additional Li^+ ions, the ionic radius of which ($\sim 0.76\text{\AA}$) is larger than that of Ni^{3+} ($\sim 0.56\text{\AA}$). In addition, the most prominent

change is observed for the (003) peak intensity, which gradually decreases relative to that of the (104) peak upon Li and Mo addition (Fig. 1a). Considering that the (003)/(104) peak intensity ratio is widely used to gauge the degree of cation mixing between the Li and M layers, we presumed that its decrease is a signature of the higher degree of cation mixing occurring upon Li and Mo incorporation.

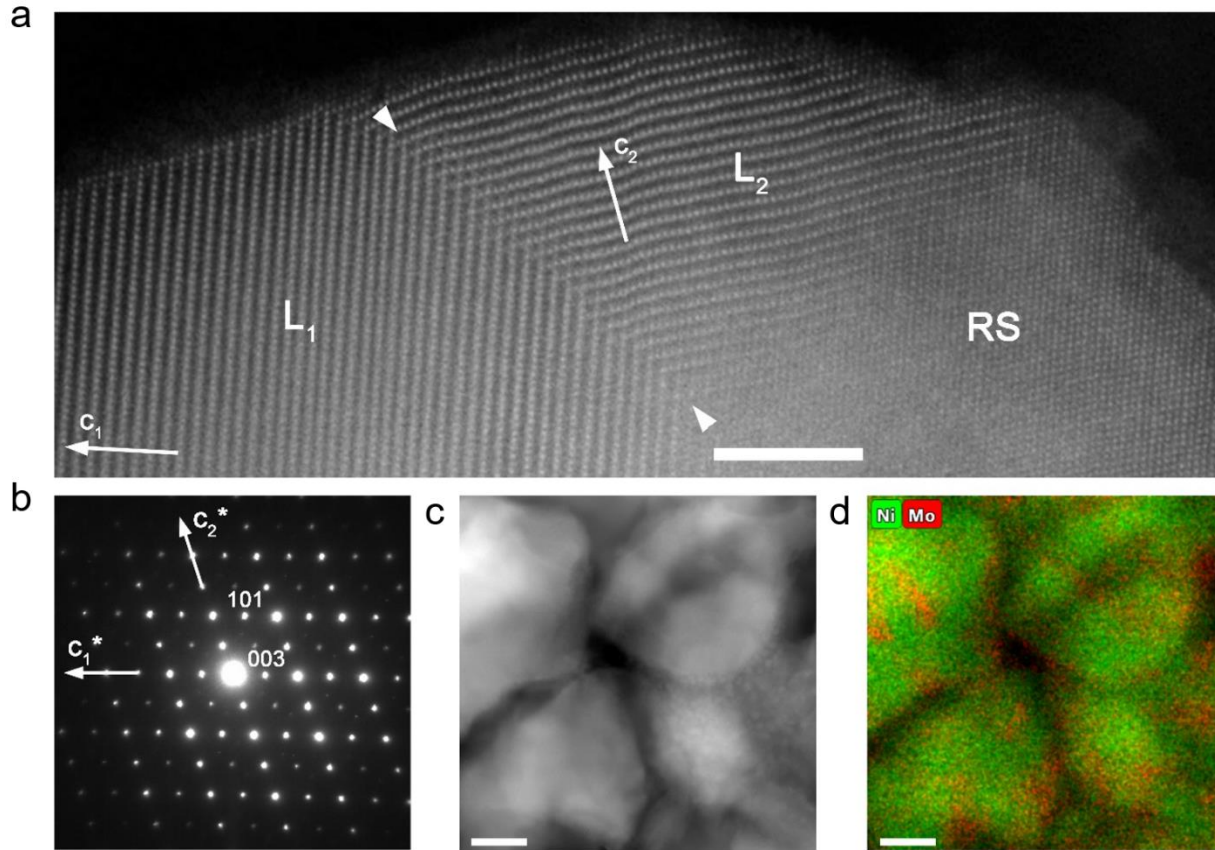


Figure 2. TEM analysis of $\text{Li}_{1.09}\text{Ni}_{0.85}\text{Mo}_{0.06}\text{O}_2$. (a) HAADF-STEM image showing the twinned domains of the layered $R\text{-}3m$ structure (L_1 and L_2) along with a disordered rock-salt (RS) domain. The orientation of the c -axis in the layered domains is marked with arrows. The (104) twin plane is traced with arrowheads. The scale bar is 5 nm. (b) ED pattern demonstrating the twinned layered O3-type structure. The reciprocal lattice axes c^* for the twinned domains are marked. (c) HAADF-STEM image and (d) the color-coded EDX map demonstrating the mosaic Ni (green) and Mo (red) distribution. The scale bar is 20 nm.

TEM analysis. Surprisingly, TEM images of the $\text{Li}_{1.09}\text{Ni}_{0.85}\text{Mo}_{0.06}\text{O}_2$ sample showed a two-phase intergrowth system rather than a solid solution. As shown in Fig. 2a,b, the high-angle annular dark-field scanning transmission electron microscopy (HAADF-STEM) image and electron diffraction (ED) pattern reveal that the O3 structure is split into twinned nanodomains separated by twin planes (marked with arrowheads in Fig. 2a; the detailed indexing of the ED

pattern is provided in Fig.S3). The transition metals and Li cations in these domains are well ordered as no HAADF intensity is observed between the brightest dots of the M columns. This indicates low fractions of Ni and Mo in the octahedral Li sites. The apparent cationic disorder in these domains is observed in the very surface layer (i.e. the thickness of one unit cell). However, next to the well-ordered layered structure, rock-salt-type disordered domains were also found, displaying a mixed distribution of the M and Li cations (marked as RS in Fig. 2a). Such a structural inhomogeneity apparently coexists with a chemical inhomogeneity as unequivocally observed from the energy dispersive X-ray (EDX) elemental mapping (Fig. 2c,d). It clearly shows a mosaic-like Mo and Ni distribution pointing toward the coexistence of a Ni-rich phase and a Mo-rich phase. The Ni:Mo atomic ratio quantified with the EDX spectra integrated over large areas (c.a. 200×200 nm) amounts to 93.3(6):6.7(6) that corresponds to $y = 0.09$, in agreement with the bulk composition of the sample determined from ICP. The Ni:Mo = 97.2(5):2.8(5) atomic ratio was measured for the Ni-rich phase that corresponds to $y = 0.04$ and hence a composition close to $\text{Li}_{1.04}\text{Ni}_{0.93}\text{Mo}_{0.03}\text{O}_2$. The domains of the Mo-rich phase are too small and overlap heavily with the Ni-rich phase, so their composition cannot be reliably determined.

NMR analysis. To explore the exact chemical structure of these intergrown phases, ^7Li NMR spectroscopy was also used as it is an excellent probe of the paramagnetic ions around lithium spins, providing access to their oxidation state and their connectivity to the observed lithium spin.

For typical Ni-based layered oxides, several Li environments can be distinguished by ^7Li NMR depending on the number and position of Ni ions interacting through Ni-O-Li bonds. As calculated in a lithium nickel cobalt oxide, each Ni^{3+} is expected to contribute to the ^7Li shift by adding -15 ppm in an edge-sharing position (Li-O-Ni angle at 90°), and +110 ppm in a corner sharing position (Li-O-Ni angle of 180°).²⁰⁻²² Those values are found to be -30 and +170 ppm for Ni^{2+} .²³ Diamagnetic ions, such as Li^+ , Mo^{6+} ($4d^0$ ion) and Co^{4+} ($3d^6$ low-spin) are expected to induce minor shift changes. These contributions would give rise to a shift of 570 ppm for a typical layered LiNiO_2 compound (6 $\text{Li}^+\text{-O-Ni}^{3+}$ at 90° and 6 $\text{Li}^+\text{-O-Ni}^{3+}$ at 180°). Nevertheless, in our case, the main LiNiO_2 peak was found at around 680 ppm (peak A in Fig. 3a), a value close to those previously measured^{22,24,25} but slightly larger than the calculated one. The discrepancy may stem from the local distortion arising around the Ni ions (Jahn-Teller) which

was absent from the structure used for the calculations. By further deconvolution of the NMR spectra, we also found an extra peak on the left-hand side of the LiNiO_2 contribution (760-780 ppm, peak B in Fig. 3) in all the samples. This peak can be assigned to the presence of Ni^{2+} ions (as in $\text{Li}_{1-z}\text{Ni}_{1+z}\text{O}_2$), which usually gives rise to larger shifts, and was also detected in a previous publication²¹ in which ^6Li MAS NMR showed a similar shoulder appearing on the left-hand side of the main peak correlating with Ni^{2+} . Interestingly, this peak (B) decreases upon Mo^{6+} addition (Fig. 3), starting at 13.4% of the total for pristine LiNiO_2 , down to 4-5% for $y=0.09$ and $y=0.12$ members.

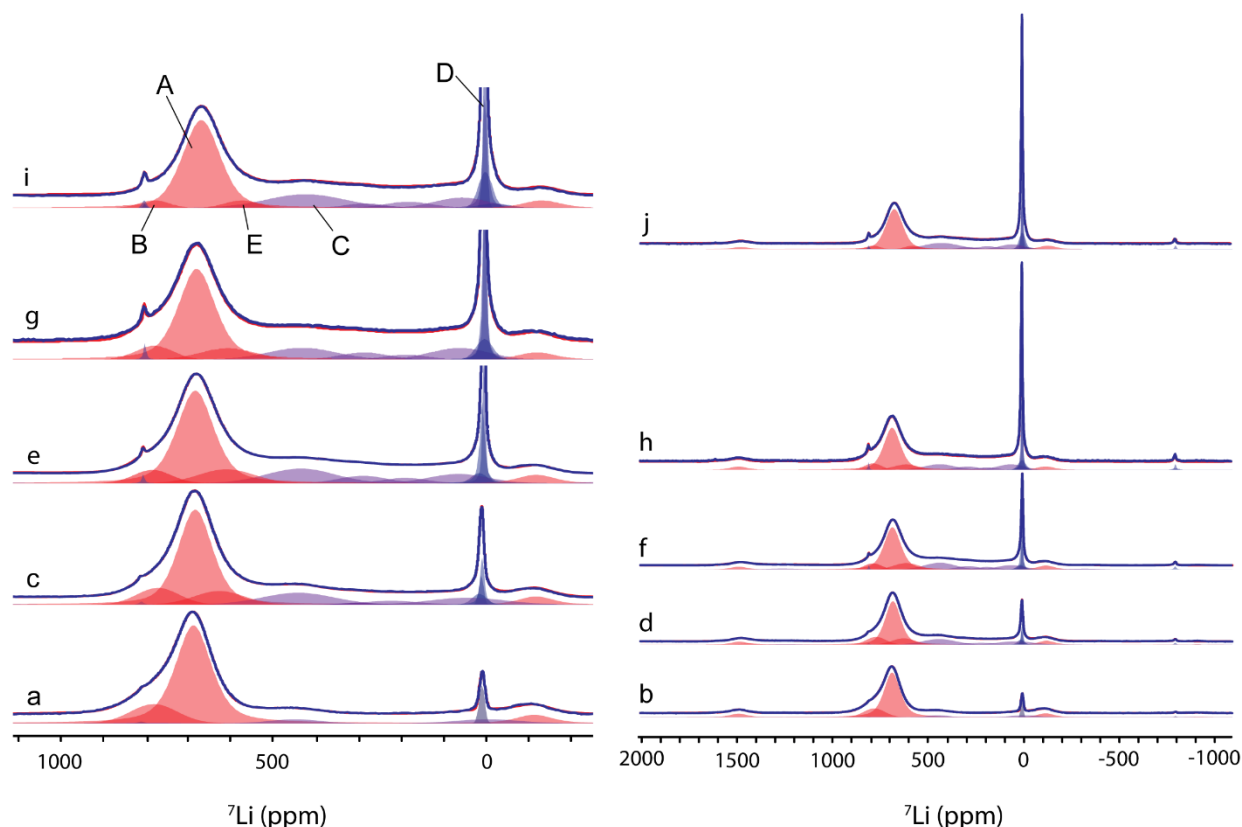


Figure 3. ^7Li MAS-NMR spectra of (a)(b) pristine LiNiO_2 , (c)(d) $\text{Li}_{1.03}\text{Ni}_{0.95}\text{Mo}_{0.02}\text{O}_2$, (e)(f) $\text{Li}_{1.06}\text{Ni}_{0.9}\text{Mo}_{0.04}\text{O}_2$, (g)(h) $\text{Li}_{1.09}\text{Ni}_{0.85}\text{Mo}_{0.06}\text{O}_2$, and (i)(j) $\text{Li}_{1.12}\text{Ni}_{0.8}\text{Mo}_{0.08}\text{O}_2$. The NMR spectra on the left hand side show the center region of the spectrum and the diamagnetic contribution (in blue) around 0 ppm is truncated. The full spectra are shown on the right hand side to illustrate the relative contributions of the diamagnetic components. The detailed results of the fits are shown in the Table S8. Different species are labelled with A, B, C, D and E corresponding to the Li signal of LiNiO_2 -rich phase, Ni^{2+} species (like in $\text{Li}_{1-z}\text{Ni}_{1+z}\text{O}_2$), Ni-rich rock salt phase, diamagnetic Li_4MoO_5 -rich phase, and less Mo^{6+} surrounded Li species, respectively.

Mo^{6+} is a d^0 diamagnetic ion, and therefore, its contribution to the shift of neighboring ^7Li spins is expected to be negligible compared to Ni^{2+} and Ni^{3+} ions. The presence of a

diamagnetic contribution (around 0 ppm, 7.9% of all lithium ions) in pristine LiNiO₂ usually stems from impurities originating from the synthesis process, i.e. lithium hydroxide or carbonate, as seen in numerous previous studies^{21,24,26}. On the other hand, an increasing diamagnetic contribution (peak D around 0 ppm in Fig. 3) that is correlated with molybdenum concentration points towards the creation of diamagnetic molybdenum and lithium-rich domains. This is confirmed by the ⁷Li T₁-relaxation behavior of this diamagnetic part, which displays long T₁ constants (≈ 1 s) compared to the T₁ of ⁷Li in the paramagnetic phase (2-5 ms), indicating that those lithium ions are far away from Ni²⁺ or Ni³⁺ ions. Considering the stoichiometry of the diamagnetic domains, one could expect a Li/Mo ratio of 4 in this phase, pointing towards Li₄MoO₅ composition. In such a case, the proportion of lithium belonging to this phase is expected to be 7.8%, 15.1%, 22.0% and 28.6% for y=0.03, 0.06, 0.09 and 0.12 samples, respectively, in good consistency with experimental ones (7.1%, 12.6%, 21.1%, and 24.1%) of the ⁷Li spins that belong to the diamagnetic domains (Table S7). The slightly less lithium than expected is not surprising, since we neglected the interface between the two domains where a Ni/Mo concentration gradient, instead of a very clear transition between the two domains, should exist. Moreover, according to EDX analysis small amount of Mo⁶⁺ is also present in the LiNiO₂ domains where some lithium ions have at least one Mo⁶⁺ as second neighbor. In both cases, new environments with intermediary shifts are created, as shown in the NMR spectra (0-400 ppm in Fig. 3), where several unassigned contributions are detected between the contribution of LiNiO₂ at 680 ppm and the diamagnetic part around 0 ppm. These peaks are referred to as “LiNi_xMo_{1-x}” species in Table S8. Based on the area ratios between bulk signal of Li₄MoO₅ and interface signal, we further quantified the Li₄MoO₅ domain sizes to be around 3.2, 4.1, 6.0 and 7.3 nm for Li_{1+y}Ni_{(3-5y)/3}Mo_{2y/3}O₂ (y=0.03, 0.06, 0.09, 0.12), respectively, as detailed in Supplementary note I. The domain size of Li_{1.09}Ni_{0.85}Mo_{0.06}O₂ is generally consistent with what we observed from STEM-EDX images in Fig. 2.

On the other hand, the detection of peaks on the right-hand side of LiNiO₂ (600-400 ppm), labelled as C and E in Fig.3 and Table S7, seem to indicate lithium ions which have one or two Mo⁶⁺ in their second coordination sphere and therefore provide more shift than lithium ions at the interface of the diamagnetic domains. Such a behavior concerns 14-20% of all lithium ions, and implies the existence of certain amount of Mo ions doped in the LiNiO₂ phase as proved by

TEM-EDX, or there is a slow transition (concentration gradient) between Li_4MoO_5 and LiNiO_2 domains.

Combining TEM with NMR results, it is clear that the exact structure of $\text{Li}_{1.09}\text{Ni}_{0.85}\text{Mo}_{0.06}\text{O}_2$ consists of a layered LiNiO_2 -rich phase and a disordered Li_4MoO_5 -rich phase. In this situation, we can now fully understand the intensity reversal of (003) and (104) diffraction peaks in XRD (Fig. 1) because of this layered-disordered intergrowth. We further used a simplified two-phase model ($R\bar{3}m$ $\text{Li}_{1.04}\text{Ni}_{0.93}\text{Mo}_{0.03}\text{O}_2$ and $Fm\bar{3}m$ Li_4MoO_5) to perform the combined refinement of the collected SXRD and NPD patterns of $\text{Li}_{1.09}\text{Ni}_{0.85}\text{Mo}_{0.06}\text{O}_2$ ($y=0.09$). As shown in Fig. 1d-e and Table S3, the refinement gave satisfying results, providing a molar ratio of 95.2(7)%:4.8(3)% for the two phases (equivalent to a composition of $\sim\text{Li}_{1.1}\text{Ni}_{0.83}\text{Mo}_{0.07}\text{O}_2$), in good consistency with the ICP-determined one.

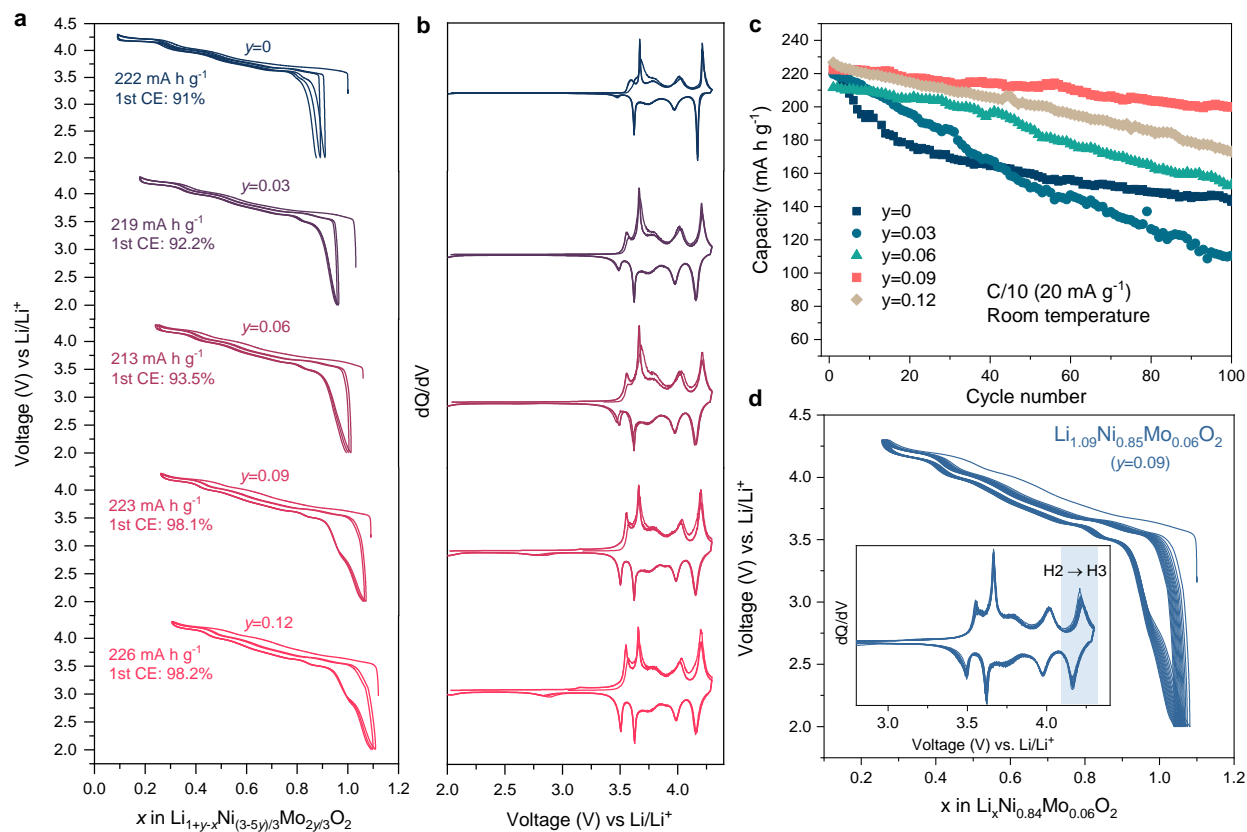


Figure 4. Electrochemistry of $\text{Li}_{1+y}\text{Ni}_{(3-5y)/3}\text{Mo}_{2y/3}\text{O}_2$ ($y=0, 0.03, 0.06, 0.09, 0.12$). (a) First three cycles of $\text{Li}_{1+y}\text{Ni}_{(3-5y)/3}\text{Mo}_{2y/3}\text{O}_2$, with their first discharge capacity and first-cycle Coulomb efficiency being noted. (b) Corresponding dQ/dV plots. (c) Cycling performance of $\text{Li}_{1+y}\text{Ni}_{(3-5y)/3}\text{Mo}_{2y/3}\text{O}_2$. For $y=0.09$ sample, 3 cells data (in light red) are shown together with average capacity and standard deviation (std.) reported (as shown by the error bar). (d) Cycling curve of $\text{Li}_{1.09}\text{Ni}_{0.85}\text{Mo}_{0.06}\text{O}_2$ with the dQ/dV plots shown as inset.

Electrochemistry. A remaining doubt regards if the disordered rock-salt domain is Li_4MoO_5 -rich phase or $\text{Li}_{1-z}\text{Ni}_{1+z}\text{O}_2$ ($z>0.38$) structure; the latter is well-known to be cation-disordered due to the similar ionic radius between Li^+ (0.76\AA) and Ni^{2+} (0.69\AA)^{19,21}. Therefore, one may consider the possibility of $\text{Li}_{1-z}\text{Ni}_{1+z}\text{O}_2$ formation upon the introduction of lithium-consumable Mo^{6+} (in forming Li_4MoO_5) that deprives the Li ions in LiNiO_2 . However, this scenario can hardly happen in our case as we simultaneously put additional Li together with Mo into the structure; as a result, the composition can be written as $\delta\text{LiNiO}_2\cdot(1-\delta)\text{Li}_4\text{MoO}_5$. Indeed, NMR results even show the decrease of $\text{Li}_{1-z}\text{Ni}_{1+z}\text{O}_2$ species (peak B in Fig. 3) upon the increase of Mo concentration.

Besides, the electrochemical response also provides crucial implications on the real structures of these electrodes. As shown in Fig. 4a, the electrochemical curves for all the samples show similar wavy characteristics with several small plateaus indicative of typical phase transitions in LiNiO_2 -based compounds. These phase transition behaviors can be more unambiguously observed from the sharp peaks in corresponding dQ/dV profiles in Fig. 4b. One specific feature worth mentioning is the sharpness of these dQ/dV peaks does not evolve too much even with decreasing Ni content. This is in stark contrast to archetypical NMC compounds, in which the Mn/Co substitution in LiNiO_2 dramatically smooths the curves and broadens the dQ/dV peaks.²⁷ This unusual feature matches well with the behavior expected for a two-phase system rather than solid solutions, as the former can largely maintain the LiNiO_2 characteristics even with increasing the Mo content. Therefore, the domain with a disordered rock-salt structure is unlikely to be the $\text{Li}_{1-z}\text{Ni}_{1+z}\text{O}_2$ ($z>0.38$) phase, as it normally appears with smoother charge/discharge curves due to the “pillar” effect of Ni^{2+} in Li layer that restrains the layer gliding and hence the phase transitions¹⁹.

To further validate the analysis above, non-Li-rich Li-Ni-Mo-O phases were also synthesized, namely, $\text{LiNi}_{1-y}\text{Mo}_y\text{O}_2$ ($y=0.02, 0.04, 0.06$, and 0.08), for comparison. As shown in Fig. S4a-d, they show similar behavior for the XRD pattern evolution — the ratio of (003)/(104) peak intensity decreases upon increasing the Mo content, though in a severer manner. However, compared to the Li-rich phases, they exhibit smoothed charge-discharge curves with much broader dQ/dV profiles (Fig. S4e-i). This, as has been referred before, implies the formation of a $\text{Li}_{1-z}\text{Ni}_{1+z}\text{O}_2$ phase in these non-Li-rich compounds since a large amount of the Li was consumed by forming Li_4MoO_5 . As a result, the non-Li-rich phase shows dramatically decreased capacity

once more Mo was added, as the $\text{Li}_{1-z}\text{Ni}_{1+z}\text{O}_2$ phase is unfavorable for Li diffusion. Therefore, these contrasts between Li-rich and non-Li-rich phases further confirm the unique intergrown structure with LiNiO_2 -rich and Li_4MoO_5 -rich (rather than $\text{Li}_{1-z}\text{Ni}_{1+z}\text{O}_2$) domains for the $\text{Li}_{1+y}\text{Ni}_{(3-5y)/3}\text{Mo}_{2y/3}\text{O}_2$ samples. It can also be inferred that the extra Li added for Li-rich compositions are mostly electrochemically active or entered into $\text{Li}_{1-z}\text{Ni}_{1+z}\text{O}_2$ lattice to form more electrochemically active LiNiO_2 domain, rather than stay on the particles surface as Li residues.

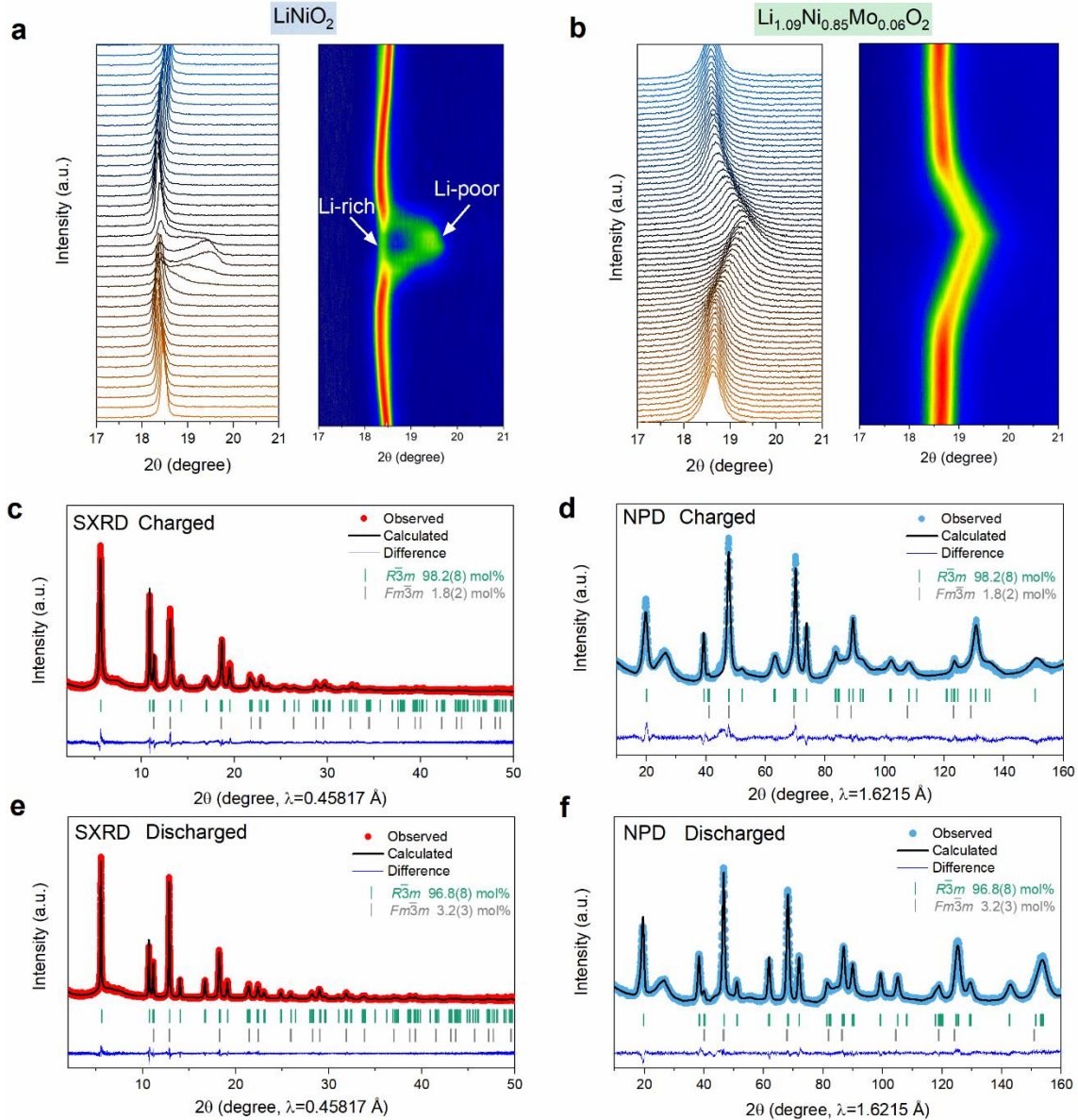


Figure 5. Intra-structural change during cycling. (a)(b) *In situ* XRD pattern ($17-21^\circ$) for LiNiO_2 and $\text{Li}_{1.09}\text{Ni}_{0.85}\text{Mo}_{0.06}\text{O}_2$, respectively, during the H2→H3 phase transition. For each compound, left side shows the patterns evolution while correspondingly, the right side shows the contour plots. Note that the peak shift looks in a less magnitude in $\text{Li}_{1.09}\text{Ni}_{0.85}\text{Mo}_{0.06}\text{O}_2$ compared with that of LiNiO_2 simply because

of the bifurcation in the latter enables more shift of Li-poor phase. (c)(d) Combined SXRD and NPD refinement results for $\text{Li}_{1.09}\text{Ni}_{0.85}\text{Mo}_{0.06}\text{O}_2$ charged to 4.3 V. (e)(f) Combined SXRD and NPD refinement results for $\text{Li}_{1.09}\text{Ni}_{0.85}\text{Mo}_{0.06}\text{O}_2$ discharged to 2.0 V.

The benefits of such “Li-rich Ni-rich” combination can be well manifested by the improved electrochemical performances. With increasing Li and Mo contents, the first-cycle Coulombic efficiency increases from 91% to around 98%, with the capacity decreasing first and then increasing to reach even higher values ($>220 \text{ mA h g}^{-1}$) at lower Ni content of 85% and 80% (Fig. 4a). Besides, the $y=0.09$ member $\text{Li}_{1.09}\text{Ni}_{0.85}\text{Mo}_{0.06}\text{O}_2$ shows an excellent capacity retention ($\sim 91\%$) after cycling at 0.1C (20 mA g^{-1}) for 100 cycles at room temperature (Fig. 4c) in stark contrast to that of pure LiNiO_2 ($\sim 64\%$). An 80% capacity retention can also be achieved for $\text{Li}_{1.09}\text{Ni}_{0.85}\text{Mo}_{0.06}\text{O}_2$ cycled at 1C (200 mA g^{-1}) for 260 cycles in a half cell versus Li, while in a full cell versus graphite it can sustain for 350 cycles at 0.5C with 87% retention (Fig. S5). It also shows quite stable cycling curves with negligible voltage decay, as observed from both the galvanostatic cycling and dQ/dV profiles in Fig. 4d. Notably, the plateau of the H2-to-H3 phase transition (shaded region in Fig. 4d), which is known for its detrimental effect to the layered structure, was retained very well upon cycling (Fig. 4d). Besides, while the addition of Li and Mo is supposed to downgrade the electronic conductivity of the compounds, $\text{Li}_{1.09}\text{Ni}_{0.85}\text{Mo}_{0.06}\text{O}_2$ shows even slightly better rate performance than that of LiNiO_2 (Fig. S6), seemingly resulting from the smaller LiNiO_2 -rich domains/particles with shorter Li diffusion paths. Moreover, the electrochemical performance of $\text{Li}_{1.09}\text{Ni}_{0.85}\text{Mo}_{0.06}\text{O}_2$ was further investigated in a wider electrochemical window (2.0-4.8V) to pursue higher capacity. Figure S7a indicates that an initial capacity of 250 mA h g^{-1} can be obtained at C/10. Though the capacity fades more quickly, it shows a small voltage hysteresis (energy efficiency: 91%) and negligible voltage decay (Fig. S7b-d), which is far more superior to typical Li-rich NMC cathodes.

Besides, differential scanning calorimetry (DSC) experiments were performed to evaluate the thermal stability of this new family of electrodes (Fig. S8). Two distinctions can be observed between bare LiNiO_2 and $\text{Li}_{1+y}\text{Ni}_{(3-5y)/3}\text{Mo}_{2y/3}\text{O}_2$ ($y=0.09$ and 0.12) samples. First, the main heat flow peak at around 210°C is very sharp and strong for LiNiO_2 , but is much suppressed for Mo-containing samples (Fig. S8). This difference corresponds well to the structural stability improvement of $\text{Li}_{1+y}\text{Ni}_{(3-5y)/3}\text{Mo}_{2y/3}\text{O}_2$ enabled by the intergrown Li_4MoO_5 -rich domains, which might restrain the structural transformation at high temperature and hence the suppressed heat flow. Second, there are additional weak heat flow peaks below 200°C in

Li_{1+y}Ni_{(3-5y)/3}Mo_{2y/3}O₂ samples but are absent in LiNiO₂. Two possibilities can explain these small peaks. One is due to the anionic redox (as will be shown later) aroused in Li_{1+y}Ni_{(3-5y)/3}Mo_{2y/3}O₂ that produces more reactive species at high voltage and temperature; second is Mo dissolution might be enhanced at elevated temperature. Both possibilities can be reasonable since, with higher Mo content, the heat release below 200°C is even increased (Fig. S8), consistent with more anionic redox contribution or more Mo dissolution triggered in high Mo-content sample.

Further shortcomings of these new class of materials in terms of electrochemical performance should be subjected to discussion. One issue is that Li_{1.09}Ni_{0.85}Mo_{0.06}O₂ shows large voltage hysteresis below 3V (Fig.4a) possibly associated with oxygen redox, as discussed later. Though, the energy efficiency can reach ~95% after initial cycles (Fig. S9), acceptable for practical application. Besides, a lower cutoff voltage down to 2.0V was used for achieving high capacities. However, even by cycling the electrode in 2.7-4.3V vs Li, the voltage window typically employed for Ni-rich materials, a capacity up to 210 mA h g⁻¹ can also be obtained with good cycling stability (Fig. S10). Moreover, while limitation do exists for Li_{1.09}Ni_{0.85}Mo_{0.06}O₂ when using a high loading (95% active materials, 10-12 mg cm⁻²) compared with low loading (80% active material, 6-8 mg cm⁻²) as shown in Fig.S11, the performance is highly promising for practical application especially considering it is Co-free.

Structural change. Since the main active phase in the intergrown structure is LiNiO₂-rich domain that bears high similarity with pure LiNiO₂ as learnt from TEM, NMR, and electrochemical studies, yet a question lingers why the former shows outstanding electrochemical stability that can hardly be achieved for the latter. First, *in situ* XRD was used to investigate their phase transition behavior during cycling. As shown in Fig. S12a, during the charge process of LiNiO₂, the (003) diffraction peak undergoes mild changes before reaching 4.2 V. However, once reaching the 4.2 V plateau corresponding to the so-called “H2→H3” phase transition, the (003) peak largely shifts towards higher angle (more than 1°), indicative of a large layer spacing shrinkage. Such a “H2→H3” phase transition is also accompanied by a very large local micro-strain as clearly observed from the very asymmetrical peak at the end of charge (Fig. S12c). Besides, in the second cycle, a bifurcation of the (003) peak emerges due to the co-existence of two phases: the Li-rich and Li-poor phases (Fig.5a and Fig. S12c). This phenomenon, previously called as “bulk fatigue” due to the formation of surface disordered rock-

330 salt phase that causes mechanical failure²⁶, is characteristic of some inactive Li ions (in Li-rich
331 phase) that are not electrochemically accessible, hence the fading of the capacity. We also
332 confirmed that this bifurcation behavior happens similarly for regularly synthesized LiNiO_2
333 (BASF) in the 2nd cycle but in lesser extent, while it largely aggravates in the 3rd cycle (Fig. S12).
334 By contrast, the (003) peak in $\text{Li}_{1.09}\text{Ni}_{0.85}\text{Mo}_{0.06}\text{O}_2$ shows less shift and less asymmetry during the
335 “H2→H3” phase transition (Fig. S12b). Specially, unlike the case of LiNiO_2 , the (003) peak of
336 $\text{Li}_{1.09}\text{Ni}_{0.85}\text{Mo}_{0.06}\text{O}_2$ remains single in the whole “H2→H3” phase transition process (Fig. 5b and
337 Fig.S12d) without any bifurcation. This implies an excellent mechanical reversibility and
338 sustainability of $\text{Li}_{1.09}\text{Ni}_{0.85}\text{Mo}_{0.06}\text{O}_2$ against LiNiO_2 , thereby explaining the huge electrochemical
339 stability contrast between these two compounds.

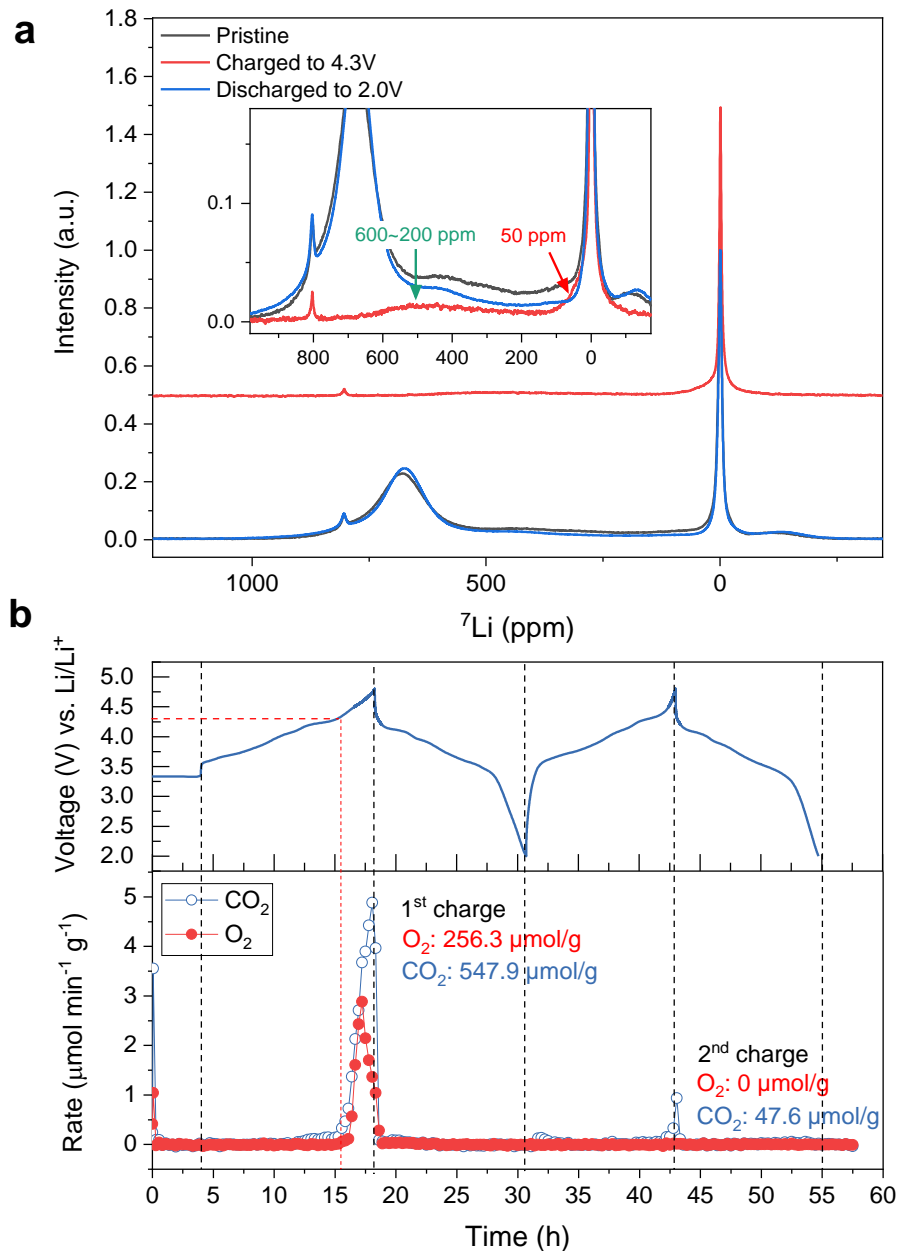


Figure 6. NMR and OEMS study during the cycling of $\text{Li}_{1.09}\text{Ni}_{0.85}\text{Mo}_{0.06}\text{O}_2$. (a) ^7Li MAS-NMR spectra of pristine (black), charged (red, top), discharged (blue) $\text{Li}_{1.09}\text{Ni}_{0.85}\text{Mo}_{0.06}\text{O}_2$. Assuming the molybdenum-rich phase is not active electrochemically, we normalized ^7Li the spectra with respect to the corresponding peak height at 0 ppm. The inset shows the enlarged view of the overlapped NMR spectra of all three samples. (b) OEMS result during the first two cycles. A red dashed line marks an onset potential of slightly above 4.3V for oxygen release at the first cycle. The amounts of O_2 and CO_2 release are indicated. CO_2 release is generally caused by electrolyte oxidation as previously reported²⁸ and further thoroughly discussed in Supplementary note II.

To further examine the intra-cycle structural change, we performed SXRD, NPD, and TEM analysis during the first cycle. The SXRD and NPD patterns of $\text{Li}_{1.09}\text{Ni}_{0.85}\text{Mo}_{0.06}\text{O}_2$ in the charged (4.3 V) and discharged (2.0 V) states were collected and analyzed with Rietveld

refinement, as shown in Fig. 5c-f and Table S4-5. The results demonstrate that the long-range cation ordering in $\text{Li}_{1.09}\text{Ni}_{0.85}\text{Mo}_{0.06}\text{O}_2$ is not significantly affected upon cycling, except that a slight deviation of the molar percentage of the Li_4MoO_5 phase is obtained in charged state but which is within the accuracy of quantitative phase analysis by Rietveld method especially considering that the peaks are fully overlapped. Absence of cation migration is also obvious from the HAADF-STEM images of $\text{Li}_{1.09}\text{Ni}_{0.85}\text{Mo}_{0.06}\text{O}_2$ in the charged and discharged states (Fig. S14). The corresponding ED patterns (insets in Fig. S14) indicate the twinned layered O3 structure is well retained. To further inspect if local structural variation exists, we collected ^7Li MAS-NMR spectra during the first cycle, as shown in Fig. 6a. Interestingly, we find that, after charge, lithium ions are mostly found in diamagnetic environments (i.e. those that are close to Mo^{6+} ions), except for a very broad component between 600 and 200 ppm (Fig. 6a inset, green arrow), and a peak at around 50 ppm (Fig. 6a inset, red arrow) which may be assigned to lithium ions at the interface of the molybdenum-rich phase. After discharge, the LiNiO_2 peak almost fully reemerges except for being slightly sharper, accompanied by a subtle intensity decrease in the range of 20-500 ppm (i.e. Li^+ ions that are close to Mo^{6+}). These results demonstrate that almost all the Li^+ from LiNiO_2 domain can be removed and can reversibly come back whereas the Li ions in Li_4MoO_5 domains are less active. Such good reversible Li intercalation chemistry in LiNiO_2 domain is in line with the high Columbic efficiency observed in $\text{Li}_{1.09}\text{Ni}_{0.85}\text{Mo}_{0.06}\text{O}_2$, hence explaining its comparable capacity with pure LiNiO_2 even with barely active Li_4MoO_5 domains in the former. Besides, the online electrochemical mass spectrometry (OEMS) experiment (Fig. 6b) shows an onset potential for oxygen release slightly above 4.3 V at the 1st charge, whereas it is totally absent during the second charge, similar to the previous reports on $\text{LiNi}_{0.8}\text{Co}_{0.1}\text{Mn}_{0.1}\text{O}_2$ ²⁸. Thus, good cycling stability is achieved by cutting off the voltage at 4.3 V, while it severely deteriorates when cycled up to 4.8 V (Fig. S7a). A SXRD pattern was also collected after cycling the sample for 50th cycles in the 2.0 - 4.3 V range (Fig. S15), showing excellent retaining of the original structure without noticeable structural disordering, as deduced from the Rietveld refinement (Table S6).

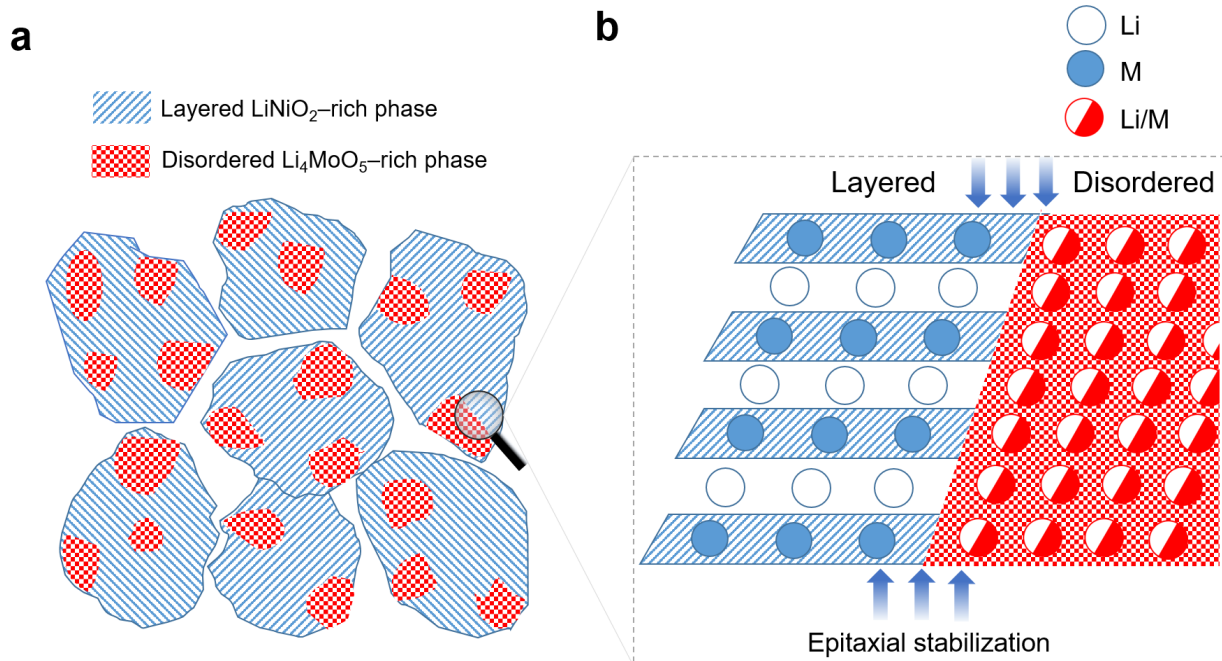


Figure 7. Schematic of the layered-disordered intergrowth of “Li-rich Ni-rich” cathode. (a) Schematic of the domains of layered LiNiO₂-rich phase and disordered Li₄MoO₅-rich phase in the grains of cathodes. (b) “Epitaxial stabilization” effect of the intergrowth in reinforcing the mechanical and structural stability of layered phase in the intergrowth structure.

The above these results collectively confirm the benefit of such two-phase intergrowth, with a Li₄MoO₅ domain sizes in the 5-20 nm range, to the structural and mechanical stability of Ni-rich oxide due to the “epitaxial stabilization” effect, as schematically shown in Fig. 7. The superimposition of the diffraction peaks (Fig. 1) of the two phases indicates the similar sub-lattice parameters and hence the coherent epitaxial interface in between the two domains (Fig. 7). As a result, the mechanical strain energy during (de)lithiation of LiNiO₂-rich phase can be largely counteracted by the epitaxial energy from Li₄MoO₅ domains, thereby decreasing the deformation and improving the cracking resistance. To simulate such effects, a calculation of free energy of the two intergrowing crystal with a coherent epitaxial interface is indeed possible with the DFT-based methods, but it requires precisely known atomic structure and chemical composition at the interface which we did not investigate in detail in this work. Without these prerequisites, the simulation results will be too speculative being based on extensive assumptions not supported by the experimental data. In our interpretation of the role of epitaxial stabilization, we refer to very recent experimental results demonstrating that epitaxial intergrowth of the layered oxide cathode material with the disordered RS-type phase helps alleviating strain during charge/discharge and greatly improve the capacity retention^{29,30}. In addition, by checking further

the redox mechanism of $\text{Li}_{1.09}\text{Ni}_{0.85}\text{Mo}_{0.06}\text{O}_2$ via XAS complemented by GITT analysis (Fig. S16), we identified a main Ni redox with a bit contribution from O redox triggered by the slight excess Li in LiNiO_2 -rich phase. A typical signature of anionic redox in this system is the large voltage hysteresis observed below 3 V, which aggravates with increasing Li and Mo contents. Such minor O redox contribution may also plays an role on the cycling stability by buffering the electron depletion of O 2p states from Ni(3d)-O(2p) σ -type interactions, as we have envisaged at the beginning.

Discussion.

We have explored here a material design strategy by combining the “Li-rich” with the “Ni-rich” concepts together, as shown by the $\text{Li}_{1+y}\text{Ni}_{(3-5y)/3}\text{Mo}_{2y/3}\text{O}_2$ family as a proof of concept. The materials display an intergrowth of a layered LiNiO_2 -rich phase and a disordered Li_4MoO_5 -based domain at the 10 nm scale rather than solid solutions. Such intergrowth of two phases, together with the minor O redox contribution, enables excellent mechanical, structural and cycling stabilities for LiNiO_2 -rich phase, thus expanding the boundary of materials design for practical high-energy-density electrodes.

The LiNiO_2 - Li_4MoO_5 intergrowth is reminiscent of previous debates on the real structure of Li-rich NMC ($(1-x)\text{Li}_2\text{MnO}_3 \cdot x\text{LiMO}_2$) compounds on whether they are solid solutions or two-phase (Li_2MnO_3 -rich and LiMO_2 -rich phases) co-existence.³¹⁻³⁶ Similarly, while their XRD patterns exhibit a single-phase feature, local fragments of Li_2MnO_3 can be frequently observed by TEM.^{32,35} An agreement seems to have been achieved that Li-rich NMCs can indeed be considered as solid solutions in the long-range scale but also show some short-range ordering of the two phases. Apparently, the structure of this class of $\text{Li}_{1+y}\text{Ni}_{(3-5y)/3}\text{Mo}_{2y/3}\text{O}_2$ compounds bears the same rationale with Li-rich NMC but with some differences. One is that Mo^{6+} is more insoluble than Mn^{4+} in LiMO_2 layered structures due to its higher valence, hence driving the phase separation of Li_4MoO_5 domains within the LiNiO_2 phase (Fig. 7a). Another is that Mo^{6+} is in d^0 electronic configuration and is more prone to forming disordered rock-salt phase in a Li-rich environment³⁷. Besides, with a 4.3 V cutoff voltage, the Li_4MoO_5 -rich phase in $\text{Li}_{1+y}\text{Ni}_{(3-5y)/3}\text{Mo}_{2y/3}\text{O}_2$ compounds is not active, as proven by NMR, unlike Li_2MnO_3 domains in Li-rich

NMC charged to 4.8 V, which is crucial to trigger anionic redox and tapping into the associated extra capacity³⁸.

Indeed, composite electrode design has been proposed by Thackeray's earlier work in Li_2MnO_3 -based compounds. Several combinations, such as "layered-rocksalt", "layered-layered", "layered-spinel" and so on, were shown to have high capacities and good cycling stabilities.^{39,40} Besides, a "layered-rocksalt" intergrown $\text{Li}_{1.2}\text{Ni}_{0.4}\text{Ru}_{0.4}\text{O}_2$ electrode was also reported recently by N. Li et al.²⁹ While these studies share a similar intergrowth structure, our work, mainly based on the "Li-rich Ni-rich" concept, provides a more practical solution for future cathode design. Besides, several pioneering studies must be mentioned, such as those led by J. Dahn, D. Aurbach, and Y.-K. Sun et al.⁴¹⁻⁴⁴, who attempted to dope $\text{Mo}^{6+}/\text{W}^{6+}$ in LiNiO_2 or its derived Ni-rich compounds, with Mo being infused in grain boundary or segregated in near surface region due to its high insolubility. Hence, our study confirms the Mo^{6+} insolubility they observed, yet it also differs by two aspects: First, in our $\text{Li}_{1+y}\text{Ni}_{(3-5y)/3}\text{Mo}_{2y/3}\text{O}_2$ series, homogenous two-phase intergrowth is achieved, rather than infused boundaries, due to our solution-based synthesis for obtaining a atomically homogeneous precursor. Such an homogeneous two-phase distribution can never been achieved with a simple solid-state synthesis even preceded by a co-precipitation step, as the mass diffusion of Mo^{6+} is difficult and Mo is more prone to precipitating in acidic solution, therefore making it impossible to co-precipitate synchronously with Ni in alkaline solution. Second, Li excess is essential to ensure the two-phase structure and the associated performance as already implied by our previous control studies (Fig. S4).

Finally, our conceptualization of "Li-rich Ni-rich" compounds can further expand the space of high-energy cathode materials design, since Mo^{6+} can be replaced by other high-valence transition metal or metalloid ions, such as W^{6+} , Te^{6+} , V^{5+} , Nb^{5+} , Sb^{5+} , Ta^{5+} , Ti^{4+} , Mn^{4+} , or Zr^{4+} etc. A preliminary study has been implemented on Ti^{4+} and Nb^{5+} systems as the representatives of tetravalent and pentavalent transition metal ion doping, showing high resemblance to the case of $\text{Li}_{1+y}\text{Ni}_{(3-5y)/3}\text{Mo}_{2y/3}\text{O}_2$ (Fig. S17). Notwithstanding, some practical parameters of these newly designed electrodes remains to be improved, such as the slightly lower tap density ($1.96(3)\text{g}\cdot\text{cm}^{-3}$) due to the smaller particle size. Future works can focus on seeking better, more abundant, high-valence M ions or combinations of those to further enhance the electrode properties. This has to be done by intensively scrutinizing the ternary composition-structure-electrochemistry relationships of these potential "Li-rich Ni-rich" materials. Besides, the impact of the synthetic

method on the microstructure at the nanometer scale and their effect on performances of the electrode remains to be further explored in pursuit of higher practicability. On solving these problems, we believe this study will pave a new way to access practical high-energy-density cathodes for Li-ion batteries.

Experimental

Materials synthesis

$\text{Li}_{1+y}\text{Ni}_{(3-5y)/3}\text{Mo}_{2y/3}\text{O}_2$ ($y=0, 0.03, 0.06, 0.09, 0.12$) and $\text{LiNi}_{1-y}\text{Mo}_y\text{O}_2$ ($y=0.02, 0.04, 0.06, 0.8$) were prepared by a solid-state process preceded by a solution step to obtain the precursors. To prepare the precursors, stoichiometric amounts of lithium acetate dihydrate (2% excess, reagent grade, Sigma-Aldrich), nickel(II) acetate tetrahydrate ($\geq 99.0\%$ (KT), Sigma-Aldrich) and $(\text{NH}_4)_6\text{Mo}_7\text{O}_{24}\cdot 4\text{H}_2\text{O}$ (ACS, 81-83% as MoO_3) were dissolved in water or ethanol, followed by drying the solution to form a viscous gel. The gel was then dried at 120°C in air for at least 8 hours, and hand ground before high-temperature annealing at 750°C under oxygen flow for 8 hours, followed by reannealing in the same condition (750°C , 8h, O_2 flow). Note that a low amount of target compound (~ 0.5 g) is easier to obtain phase-pure, whereas scaling up will sometimes lead to easily detected impurities (mainly Li_4MoO_5), as observed from XRD.

Electrochemistry

Electrochemical studies were done in 2032-type coin cells unless otherwise specified. 80 wt.% of active materials with 20 wt.% carbon (Super P) were homogeneously mixed together as cathode electrodes. The coin cells were assembled with the cathode powder (with a loading of 6-8 mg/cm^2) countered by a Li foil as the anode, between which two Whatman GF/D borosilicate glass fiber sheets were used as the separator. LP 57 electrolyte (1M LiPF_6 in EC/EMC= 30:70 wt.%) mixed with 2 wt.% vinylene carbonate (VC) was used as electrolyte for cycling between 2.0 and 4.3 V, whereas a LP30 electrolyte (1M LiPF_6 in EC/DMC= 50:50 wt.%, E-Lyte) was used for cycling between 2.0 and 4.8 V.

General characterization (ICP, XRD, NPD, SEM and DSC).

The ICP-AES data was collected with a PerkinElmer NexION 2000 ICP mass spectrometer, and the samples were first dissolved with *aqua regia* and then adjusted to appropriate concentrations with deionized water in a volumetric flask before the measurements. XRD patterns were obtained via a laboratory X-ray diffractometer (BRUKER D8 Advance) equipped with a $\text{Cu K}\alpha$ radiation source ($\lambda_{\text{K}\alpha 1} = 1.54056 \text{ \AA}$, $\lambda_{\text{K}\alpha 2} = 1.54439 \text{ \AA}$) and a Lynxeye XE detector. A homemade airtight cell with a beryllium window was used for *in situ* XRD experiments, for which the electrochemistry was ran synchronously with data acquisition. Constant-wavelength NPD data were collected at room temperature on the WOMBAT high intensity neutron powder diffractometers, with the sample sealed under Argon, using a wavelength of 1.6215 \AA . All the Rietveld refinements of the XRD and NPD patterns were done with the FullProf program⁴⁵. SEM images were obtained on an FEI Magellan scanning electron microscope equipped with an Oxford Instruments energy dispersive X-ray spectroscopy (EDX) detector. EDX was carried out using an acceleration voltage of 20 kV. DSC experiments were carried out with a Mettler Toledo TGA/DSC 3+ (LF 1100 $^\circ\text{C}$) equipment at a rate of 5°C min^{-1} between 25 and 300°C under a constant Ar gas flow. The samples for DSC were charge to 4.3 V and recovered, washed by DMC for three times, and then dried under vacuum. The tests were conducted by soaking the 3~5 mg dried samples into 100 μl LP57 electrolyte and sealed in an aluminum crucible.

TEM

Samples for transmission electron microscopy (TEM) were prepared in an Ar-filled glovebox by grinding the powders in an agate mortar in dimethyl carbonate and depositing drops of suspension onto copper TEM grid with holey carbon support layer. The sample was transported to the TEM column by means of a Gatan vacuum transfer holder completely avoiding contact with air and moisture. Electron diffraction (ED) patterns, high angle annular dark field scanning transmission electron microscopy (HAADF-STEM) images and energy-dispersive X-ray (EDX) spectra were collected with a probe-corrected Titan Themis Z electron microscope operated at 200 kV and equipped with a Super-X EDX detector.

OEMS

Freestanding electrodes comprised 70% wt. active materials, 20% wt. carbon (Super P) and 10% PTFE were used. An in-house designed OEMS cell⁴⁶ was used to run the experiment. 150 μ L of LP30 electrolyte, Li foil as anode and 1 piece of GF/D glassfiber separator were used to assemble the half-cell. The quantitative gas evolution data on m/z channels of 32 (O_2) and 44 (CO_2) was collected using an *operando* protocol where the cell was rested for 4 h before and 12 h after the full electrochemistry cycle to stabilize the background signal. The OEMS cells were cycled in the 2.0 - 4.8 V range for two cycles at a C/10 rate (20 mA g^{-1}). At least two cells were tested to ensure results reproducibility.

XAS

Ni K-edge and Mo K-edge XAS spectra were collected in transmission mode at ROCK⁴⁷ beamline of the SOLEIL synchrotron facility at Paris, France. A Si(111) channel-cut quick-XAS monochromator with an energy resolution of 0.7 eV at 7 keV was used. The intensity of the monochromatic X-ray beam was measured using three consecutive ionization detectors. For sample preparation, powders (80% active material and 20% carbon super P) were cycled to specific states of charge and then recovered, washed with DMC for three times, and finally dried under reduced pressure. Then the dried powders were mixed with certain amount of cellulose, and pressed as thin pellets. The pellets were sealed carefully into X-ray transparent plastic bags before taking to XAS measurements. The energy calibration was performed using Ni and Mo foils placed between the second and third ionization chambers. All XAS data were processed with the Athena program⁴⁸.

NMR

Solid-state NMR experiments were performed on a 4.7 T Avance III HD Bruker NMR spectrometer (200 MHz for 1H , 77.8 MHz for 7Li , 29.4 MHz for 6Li), using a 1.3 mm magic angle spinning (MAS) probe spinning at 62.5 kHz under pure nitrogen gas. Without temperature regulation, the temperature inside the rotor is expected to be around 50°C. All 7Li NMR experiments were recorded with a rotor-synchronized Hahn echo sequence, and the 90° pulse was set to 1.1 μ s and the chemical shift was referenced with liquid 7LiCl in water at 0 ppm (corresponding to a 227 kHz B_1 field strength). The T_1 relaxation times were measured using a saturation-recovery experiment, using 20 x 90° pulses separated by a 1 ms delay for saturation. The T_1 behavior was found to be mono-exponential for the left hand side peaks (around 600-850 ppm) and the T_1 values were around 2-5 ms, as expected for 7Li spins close to paramagnetic Ni^{3+} ions. For the diamagnetic part, the T_1 relaxation was found to be multiexponential, with at least two components, a slow relaxing component with T_1 values between 1 and 1.5 seconds, while a fast relaxing component was observed with T_1 values between 5 and 30ms. This is expected as, first, the spinning sideband from the $LiNiO_2$ peak overlaps with the 0 ppm contribution (fitted in red, on the right hand side, around -120 ppm); second, the diamagnetic contribution is made of lithium in molybdenum-rich domains, embedded in the $LiNiO_2$ phase, and therefore, lithium ions close to the interface will display shorter relaxation times. Therefore, all 7Li spectra were recorded using a 5 to 10 s relaxation delays to ensure a

proper quantification of the diamagnetic contribution, with at least 1024 transients recorded to ensure a sufficient signal-to-noise ratio. The ^6Li Hahn echo experiment was obtained with a 90° pulse of $2.1\ \mu\text{s}$ duration, and a 50 ms recovery delay was used, allowing for the recovery of the magnetization of the ^6Li close to Ni ions. However, the experiment is not quantitative for the slow relaxing ^6Li spins in the diamagnetic phase, and 675,504 transients were recorded to obtain a good signal-to-noise ratio. The ^6Li NMR spectrum was recorded to confirm that no peak was overlapping with the spinning sidebands that are observed in the ^7Li spectrum, as shown in Figure S18. The spectra were deconvoluted with dmfit, using the minimum number of necessary Gausso-Lorentzian spinning sideband patterns (5 spinning sidebands maximum) characterized by a Gaussian/Lorentzian ratio, a position (in ppm), a width (in ppm), and an intensity, all of which were fitted by the program.⁴⁹ The spinning sidebands intensities were fitted (no model was used) independently, and the relative weight of each contribution was obtained from the area of the whole spinning sideband pattern. Special care was taken to measure NMR spectra on fresh samples with as little contact as possible with residual moisture in the glovebox or in the NMR spectrometer.

ACKNOWLEDGMENTS

This research used resources of the Advanced Photon Source, a US Department of Energy (DOE) Office of Science User Facility, operated for the DOE Office of Science by Argonne National Laboratory under Contract No. DE-AC02-06CH11357. We are grateful to Tuncay Koç for his kind help in performing SEM and EDX measurements, to Valentin Meunier and Ivette Aguilar for their kind help in measuring ICP, to Antonella Iadecola for her help in collecting the XAS spectra, and to Sathiya Mariyappan for her kind help in performing the DSC measurements. A.M.A. is grateful to the Russian Science Foundation for financial support (grant 20-13-00233). Access to TEM facilities was granted by the Advance Imaging Core Facility of Skoltech. J.-M.T and B.L. acknowledge funding from the European Research Council (ERC) (FP/2014)/ERC Grant-Project 670116-ARPEMA.

AUTHOR CONTRIBUTIONS

B.L. and J.-M.T. conceived the idea and designed the experiments. B.L. carried out the synthesis, structural characterization and electrochemical analysis. G.R. did the analysis of SXRD and NPD data. M.A. collected the NPD patterns. A.M.A. performed TEM experiments and did the analysis. L.Z. did the OEMS experiments and data analysis. M.D. collected NMR data and did the analysis. B.L. and J.-M.T. wrote the manuscript with the contributions from all the authors.

DECLARATION OF INTERESTS

The “Li-rich Ni-rich” materials are patented by Collège de France and Umicore (inventors B.L. and J.-M.T.) with patent application number A22012-EP-EPA and A22012-EP-EPA2 (pending).

REFERENCES

1. IEA (2020), Global EV Outlook 2020, IEA, Paris <https://www.iea.org/reports/global-ev-outlook-2020>.
2. M. S. Whittingham, *Chemical Reviews*, 2004, **104**, 4271-4302.
3. P. Rozier and J. M. Tarascon, *Journal of The Electrochemical Society*, 2015, **162**, A2490-A2499.
4. G. Assat and J.-M. Tarascon, *Nature Energy*, 2018, **3**, 373-386.
5. B. Li and D. Xia, *Advanced materials*, 2017, **29**.
6. M. Zhang, D. A. Kitchaev, Z. Lebens-Higgins, J. Vinckeviciute, M. Zuba, P. J. Reeves, C. P. Grey, M. S. Whittingham, L. F. J. Piper, A. Van der Ven and Y. S. Meng, *Nature Reviews Materials*, 2022.
7. M. Li, T. Liu, X. Bi, Z. Chen, K. Amine, C. Zhong and J. Lu, *Chem Soc Rev*, 2020, **49**, 1688-1705.
8. B. Li and J.-M. Tarascon, 2022.
9. S.-T. Myung, F. Maglia, K.-J. Park, C. S. Yoon, P. Lamp, S.-J. Kim and Y.-K. Sun, *ACS Energy Letters*, 2017, **2**, 196-223.
10. W. Li, E. M. Erickson and A. Manthiram, *Nature Energy*, 2020, **5**, 26-34.
11. S. S. Zhang, *Energy Storage Materials*, 2020, **24**, 247-254.
12. J. Liu, Z. Du, X. Wang, S. Tan, X. Wu, L. Geng, B. Song, P.-H. Chien, S. M. Everett and E. Hu, *Energy & Environmental Science*, 2021.
13. A. O. Kondrakov, H. Geßwein, K. Galdina, L. de Biasi, V. Meded, E. O. Filatova, G. Schumacher, W. Wenzel, P. Hartmann, T. Brezesinski and J. Janek, *The Journal of Physical Chemistry C*, 2017, **121**, 24381-24388.
14. M. Dixit, B. Markovsky, F. Schipper, D. Aurbach and D. T. Major, *The Journal of Physical Chemistry C*, 2017, **121**, 22628-22636.
15. H. H. Sun, U.-H. Kim, J.-H. Park, S.-W. Park, D.-H. Seo, A. Heller, C. B. Mullins, C. S. Yoon and Y.-K. Sun, *Nature Communications*, 2021, **12**, 6552.
16. C.-H. Jung, Q. Li, D.-H. Kim, D. Eum, D. Ko, J. Choi, J. Lee, K.-H. Kim, K. Kang, W. Yang and S.-H. Hong, *Journal of Materials Chemistry A*, 2021, **9**, 17415-17424.
17. C. Zhang, J. Wan, Y. Li, S. Zheng, K. Zhou, D. Wang, D. Wang, C. Hong, Z. Gong and Y. Yang, *Journal of Materials Chemistry A*, 2020, **8**, 6893-6901.
18. T. P. Dadze, G. A. Kashirtseva, M. P. Novikov and A. V. Plyasunov, *Fluid Phase Equilibria*, 2017, **440**, 64-76.
19. M. Bianchini, M. Roca-Ayats, P. Hartmann, T. Brezesinski and J. Janek, *Angewandte Chemie*, 2019, **58**, 10434-10458.
20. C. Marichal, J. Hirschinger, P. Granger, M. Menetrier, A. Rougier and C. Delmas, *Inorganic Chemistry*, 1995, **34**, 1773-1778.
21. C. Chazel, M. Ménétrier, L. Croguennec and C. Delmas, *Magnetic Resonance in Chemistry*, 2005, **43**, 849-857.
22. D. Carlier, M. Ménétrier, C. P. Grey, C. Delmas and G. Ceder, *Physical Review B*, 2003, **67**, 174103.

- 629 23. D. Zeng, J. Cabana, J. Bréger, W.-S. Yoon and C. P. Grey, *Chemistry of Materials*, 2007, **19**,
630 6277-6289.
- 631 24. C. Chazel, M. Ménétrier, L. Croguennec and C. Delmas, *Inorganic Chemistry*, 2006, **45**, 1184-
632 1191.
- 633 25. H. Li, W. Hua, X. Liu-Théato, Q. Fu, M. Desmau, A. Missyul, M. Knapp, H. Ehrenberg and S.
634 Indris, *Chemistry of Materials*, 2021, **33**, 9546-9559.
- 635 26. C. Xu, K. Marker, J. Lee, A. Mahadevegowda, P. J. Reeves, S. J. Day, M. F. Groh, S. P. Emge, C.
636 Ducati, B. Layla Mehdi, C. C. Tang and C. P. Grey, *Nature materials*, 2021, **20**, 84-92.
- 637 27. N. Zhang, J. Li, H. Li, A. Liu, Q. Huang, L. Ma, Y. Li and J. R. Dahn, *Chemistry of Materials*,
638 2018, **30**, 8852-8860.
- 639 28. D. Streich, C. Erk, A. Guéguen, P. Müller, F.-F. Chesneau and E. J. Berg, *The Journal of*
640 *Physical Chemistry C*, 2017, **121**, 13481-13486.
- 641 29. N. Li, M. Sun, W. H. Kan, Z. Zhuo, S. Hwang, S. E. Renfrew, M. Avdeev, A. Huq, B. D.
642 McCloskey, D. Su, W. Yang and W. Tong, *Nature Communications*, 2021, **12**, 2348.
- 643 30. D. P. Singh, Y. A. Birkhölzer, D. M. Cunha, T. Dubbelink, S. Huang, T. A. Hendriks, C. Lievens
644 and M. Huijben, *ACS Applied Energy Materials*, 2021, **4**, 5024-5033.
- 645 31. H. Yu, R. Ishikawa, Y. G. So, N. Shibata, T. Kudo, H. Zhou and Y. Ikuhara, *Angewandte Chemie*,
646 2013, **52**, 5969-5973.
- 647 32. Z. Lu, L. Y. Beaulieu, R. A. Donaberger, C. L. Thomas and J. R. Dahn, *Journal of The*
648 *Electrochemical Society*, 2002, **149**, A778.
- 649 33. K. A. Jarvis, Z. Deng, L. F. Allard, A. Manthiram and P. J. Ferreira, *Chemistry of Materials*, 2011,
650 **23**, 3614-3621.
- 651 34. S. H. Kang, P. Kempgens, S. Greenbaum, A. J. Kropf, K. Amine and M. M. Thackeray, *Journal*
652 *of Materials Chemistry*, 2007, **17**, 2069-2077.
- 653 35. C. H. Lei, J. Bareño, J. G. Wen, I. Petrov, S. H. Kang and D. P. Abraham, *Journal of Power*
654 *Sources*, 2008, **178**, 422-433.
- 655 36. D. Mohanty, A. Huq, E. A. Payzant, A. S. Sefat, J. Li, D. P. Abraham, D. L. Wood and C. Daniel,
656 *Chemistry of Materials*, 2013, **25**, 4064-4070.
- 657 37. A. Urban, A. Abdellahi, S. Dacek, N. Artrith and G. Ceder, *Phys Rev Lett*, 2017, **119**, 176402.
- 658 38. G. Assat, D. Foix, C. Delacourt, A. Iadecola, R. Dedryvere and J. M. Tarascon, *Nat Commun*,
659 2017, **8**, 2219.
- 660 39. J. R. Croy, S. H. Kang, M. Balasubramanian and M. M. Thackeray, *Electrochemistry*
661 *Communications*, 2011, **13**, 1063-1066.
- 662 40. M. M. Thackeray, C. S. Johnson, J. T. Vaughey, N. Li and S. A. Hackney, *Journal of Materials*
663 *Chemistry*, 2005, **15**, 2257-2267.
- 664 41. U. H. Kim, D. W. Jun, K. J. Park, Q. Zhang, P. Kaghazchi, D. Aurbach, D. T. Major, G. Goobes,
665 M. Dixit, N. Leifer, C. M. Wang, P. Yan, D. Ahn, K. H. Kim, C. S. Yoon and Y. K. Sun, *Energy*
666 *& Environmental Science*, 2018, **11**, 1271-1279.
- 667 42. C. Geng, D. Rathore, D. Heino, N. Zhang, I. Hamam, N. Zaker, G. A. Botton, R. Omessi, N.
668 Phattharasupakun, T. Bond, C. Yang and J. R. Dahn, *Advanced Energy Materials*, 2021, 2103067.
- 669 43. G.-T. Park, D. R. Yoon, U.-H. Kim, B. Namkoong, J. Lee, M. M. Wang, A. C. Lee, X. W. Gu, W.
670 C. Chueh, C. S. Yoon and Y.-K. Sun, *Energy & Environmental Science*, 2021, **14**, 6616-6626.
- 671 44. D. Rathore, C. Geng, N. Zaker, I. Hamam, Y. Liu, P. Xiao, G. A. Botton, J. Dahn and C. Yang,
672 *Journal of The Electrochemical Society*, 2021, **168**, 120514.
- 673 45. J. Rodríguez-Carvajal, *Physica B: Condensed Matter*, 1993, **192**, 55-69.
- 674 46. L. Zhang, C. Tsolakidou, S. Mariyappan, J.-M. Tarascon and S. Trabesinger, *Energy Storage*
675 *Materials*, 2021, **42**, 12-21.
- 676 47. V. Briois, C. La Fontaine, S. Belin, L. Barthe, T. Moreno, V. Pinty, A. Carcy, R. Girardot and E.
677 Fonda, *Journal of Physics: Conference Series*, 2016, **712**, 012149.
- 678 48. B. Ravel and M. Newville, *Journal of Synchrotron Radiation*, 2005, **12**, 537-541.

- 679 49. D. Massiot, F. Fayon, M. Capron, I. King, S. Le Calvé, B. Alonso, J.-O. Durand, B. Bujoli, Z.
680 Gan and G. Hoatson, *Magnetic Resonance in Chemistry*, 2002, **40**, 70-76.